

Structural characterization and functional correlation of Fe<sub>3</sub>O<sub>4</sub> nanocrystals obtained using 2-ethyl-1,3-hexanediol as innovative reactive solvent in non-hydrolytic sol-gel synthesis

*Original*

Structural characterization and functional correlation of Fe<sub>3</sub>O<sub>4</sub> nanocrystals obtained using 2-ethyl-1,3-hexanediol as innovative reactive solvent in non-hydrolytic sol-gel synthesis / Sciancalepore, Corrado; Gualtieri, Alessandro F.; Scardi, Paolo; Flor, Albert; Allia, Paolo; Tiberto, Paola; Barrera, Gabriele; Messori, Massimo; Bondioli, Federica. - In: MATERIALS CHEMISTRY AND PHYSICS. - ISSN 0254-0584. - STAMPA. - 207:(2018), pp. 337-349. [10.1016/j.matchemphys.2017.12.089]

*Availability:*

This version is available at: 11583/2700911 since: 2018-02-22T14:12:07Z

*Publisher:*

Elsevier Ltd

*Published*

DOI:10.1016/j.matchemphys.2017.12.089

*Terms of use:*

This article is made available under terms and conditions as specified in the corresponding bibliographic description in the repository

*Publisher copyright*

Elsevier postprint/Author's Accepted Manuscript

© 2018. This manuscript version is made available under the CC-BY-NC-ND 4.0 license  
<http://creativecommons.org/licenses/by-nc-nd/4.0/>. The final authenticated version is available online at:  
<http://dx.doi.org/10.1016/j.matchemphys.2017.12.089>

(Article begins on next page)

# Structural characterization and functional correlation of Fe<sub>3</sub>O<sub>4</sub> nanocrystals obtained using 2-ethyl-1,3-hexanediol as innovative reactive solvent in non-hydrolytic sol-gel synthesis

Corrado Sciancalepore<sup>a</sup>, Alessandro F. Gualtieri<sup>b</sup>, Paolo Scardi<sup>c</sup>, Albert Flor<sup>c</sup>, Paolo Allia<sup>d</sup>, Paola Tiberto<sup>e</sup>, Gabriele Barrera<sup>e</sup>,  
Massimo Messori<sup>f</sup>, Federica Bondioli<sup>a,g</sup>

<sup>a</sup>INSTM, Research Unit of Parma, Department of Engineering and Architecture, University of Parma, Parco Area delle Scienze 181/A, 43124, Parma, Italy

<sup>b</sup>Department of Chemical and Earth Sciences, University of Modena and Reggio Emilia, Via Campi 103, 41125, Modena, Italy

<sup>c</sup>Department of Civil, Environmental & Mechanical Engineering, University of Trento,  
via Mesiano 77, 38123 Trento, Italy

<sup>d</sup>Department of Applied Science and Technology, Polytechnic University of Torino, Corso Duca degli Abruzzi 24, 10129, Torino, Italy

<sup>e</sup>I.N.Ri.M., Electromagnetism, Strada delle Cacce 91, 10138, Torino, Italy

<sup>f</sup>Department of Engineering “Enzo Ferrari”, University of Modena and Reggio Emilia, Via Vivarelli 10, 41125 Modena, Italy

<sup>g</sup>Department of Engineering and Architecture, University of Parma, Parco Area delle Scienze 181/A, 43124, Parma, Italy

## Abstract

An original non-hydrolytic sol-gel approach, using 2-ethyl-1,3-hexanediol as reactive solvent, was proposed to synthesize nanostructured magnetite. Iron-oxide nanoparticles were prepared and studied as a function of the precursor-to-solvent ratio. The crystallization degree of nanoparticles was followed by the combined Rietveld and Reference Intensity Ratio method. This procedure has allowed the determination of both amorphous and crystalline content of nanomagnetite, using hematite as suitable internal standard. The results of Rietveld method show that the crystalline content decreases as the precursor-to-solvent is increased, ranging from 67 to 60 wt%. Information on the crystallite size-strain distribution and microstructural evolution of nanocrystals was supplied by line profile analysis of the powder diffraction patterns, employing the Whole Powder Pattern Modeling analysis: the obtained log-normal distribution curves become increasingly narrow and symmetrical, while nanoparticle microstrain increases as the precursor concentration is increased. The dimensional analysis of the Transmission Electron Microscopy images has allowed to obtain the nanoparticle grain-size distribution. Nanoparticle dimensions decreases from 15 to 9 nm increasing the precursor concentration. The comparison between the results of X-ray diffraction and microscopic characterization techniques highlighted the effect of several factors, such as size, shape and microstructure of magnetite nanoparticles, on their functional magnetic response. Magnetic characterizations show that magnetite nanoparticles are not in the superparamagnetic phase even at room temperature, independent of the precursor concentration. On the other hand, the room-temperature saturation magnetization, ranging from 73 to 60 emu/g, is a function of the nanoparticle average size, decreasing as the precursor concentration increases.

**Key words:** Nano-magnetite; non-hydrolytic sol gel; Rietveld-RIR method; Whole Powder Pattern Modeling; interactive superparamagnetic nanoparticles

## 1. Introduction

At the nanoscale, the fundamental magnetic properties, such as the blocking temperature, the spin life time, the coercivity, the susceptibility and saturation magnetization, are no longer permanent characteristics of the materials and are strongly influenced by size, shape, composition and microstructure of the nanoparticles [1]. In fact, down to 100 nm the characteristics of solids are progressively altered and defined by the quantum size effect, which controls many physical

aspects, such as optoelectronic and magnetic ones [2,3].

Such size effect on magnetic response has been well demonstrated in the case of iron-oxide nanoparticles [4] and results in the scaling laws, which can be used to tune the magnetic peculiarities of the nanoparticles and nanostructures [5-8], in order to obtain a precise set of performance [9-11], generally higher or at least not comparable to those exhibited by conventional bulk materials.

For this reason, considerable research attention has been placed to the preparation of magnetite ( $\text{Fe}_3\text{O}_4$ ) nanoparticles, due to their potential applications, ranging from biomedicine (biosensing, magnetic imaging, drug delivery and magnetic hyperthermia) [12] to environmental (sensitive detection of specific analytes, water treatment with high gradient magnetic separation and bioremediation)[13] and data storage technologies (electromagnetic memory devices) [14,15].

Methods to synthesize magnetic nanoparticles with useful functional properties have been extensively reviewed in the last few years [16-18]. In fact the synthesis method plays a key role in the preparation of magnetic nanoparticles in terms of purity, reproducibility and desired magnetic performances. In this frame, the synthesis in organic solvents seems to be particularly suitable for the preparation of magnetic metal-oxide nanoparticles [19].

Wet chemical methods in non-aqueous environment offer high flexibility in terms of nanosized crystallite dimensions, narrow particle size distributions, well-defined morphology and microstructure of nanoparticles, while providing high compositional homogeneity [20,21]. In particular the Non-Hydrolytic Sol-Gel (NHSG) approach is based on the reaction of the precursor species (inorganic metal salts, alkoxides, acetates and acetylacetonates) with an organic solvent (alcohols, amines or ketones), allowing the preparation of a wide variety of nanocrystalline binary [22] and ternary metal oxides [23]. Monofunctional alcohols, such as benzyl alcohol, are the most common solvents used in NHSG syntheses [24,25]. Bi- or poly- functional alcohols, instead, are less conventional as suitable solvents for synthesis in non-aqueous environment.

In this work, magnetic iron-oxide nanoparticles (MNPs) was prepared by one-step NHSG reaction between iron(III)-acetylacetonate, as metal precursor, and 2-ethyl-1,3-hexanediol, a bifunctional alcohols used for the first time to the best knowledge of the authors, as reactive solvent. This approach provides a simple solvothermal way to obtain well crystallized  $\text{Fe}_3\text{O}_4$  nanoparticles with controlled size and tunable magnetic properties. To understand the correlation between the functional and the structural properties, required to design and build novel electronic, magnetic and optoelectronic devices, the obtained MNPs were characterized in detail as a function of the precursor to solvent ratio that directly influences the crystallization process and the final size, morphology and magnetic behavior of nanoparticles. In fact, it is very well known that the MNPs magnetic properties are affected by several factors including size, shape, actual chemical composition [26], interactions and degree of aggregation [27].

In the present work, the results of XRD, TEM and magnetic characterization techniques were combined in order to understand the relationship between the microstructure and the chemical and physical properties of the nanostructured material. In particular, the evaluation of the effect of the precursor-to-solvent ratio on both microstructure and crystallinity degree was carried out by X-ray diffraction (XRD) and transmission electron microscopy (TEM). Structure of the MNPs and quantitative phase analysis (QPA), including the evaluation of the amorphous fraction, were determined by the combination of the Rietveld [28] and Reference Intensity Ratio (R.I.R.) methods [29-31], using hematite as internal standard [32]. The MNPs microstructure, a fundamental notion that comprises all aspects of the atomic arrangement that should be known in order to understand the material properties, was studied, starting from the X-ray diffraction patterns, using the Whole Powder Pattern Modeling (WPPM) procedure [33,34]. Unlike the traditional methods based on the determination of the integral breadth of the line profiles, more information can be obtained from the analysis of the whole

diffraction pattern, including the crystallite size distribution and the lattice deformation.

The obtained results were correlated to room-temperature magnetic data, complemented by low-temperature measurements, to get a detailed picture of the considered nanoparticles and to understand the effect of several factors, such as size, shape and microstructure, on the functional magnetic response of the synthesized Fe<sub>3</sub>O<sub>4</sub> nanoparticles.

## 2. Experimental section

### 2.1 Synthesis of magnetite nanoparticles

Acetylacetone (AcAcH, Carlo Erba, Milan, I), iron (III) chloride hexahydrate (FeCl<sub>3</sub>·6H<sub>2</sub>O, Carlo Erba, Milan, I), sodium acetate (CH<sub>3</sub>COONa, Sigma Aldrich) and ethyl alcohol (EtOH, Sigma Aldrich) were used to synthesize the precursor iron(III)-acetylacetonate (Fe(AcAc)<sub>3</sub>), as reported in Messori et al. [35]. To evaluate the effect of the precursor-to-solvent ratio on the nanoparticle properties, 1.00 g of Fe(AcAc)<sub>3</sub> was dissolved in a 100 mL Schlenk tube in different amounts of 2-ethyl-1,3-hexanediol (HD, Sigma Aldrich). The syntheses were performed at 200 °C for 48 h with molar ratio of 0.04, 0.09, 0.18 and 0.27 mol/mol (see composition details in Table 1). The experimental synthesis setup was adapted from previous work of Pinna et al. [36] on the synthesis of MNPs, starting from Fe(AcAc)<sub>3</sub> and benzyl alcohol. The reaction starts with the thermal solvolysis of Fe(AcAc)<sub>3</sub>, followed by aldol condensation reaction, that leads to the formation of a Fe-OH species, representing the starting point of nanoparticle formation. The mechanism for the reaction of Fe(AcAc)<sub>3</sub> in HD is depicted in [37]. The products were washed by repeated centrifugation (4000 rpm for 60 min) and redispersion in methanol, until the liquid phase appeared colorless. The washed particles were finally dried under reduced pressure at room temperature and kept in closed containers until analyzed.

### 2.2 XRD data collection and analysis

A Bragg–Brentano  $\theta$ -2 $\theta$  diffractometer (X'Pert PRO PANalytical, Netherlands), equipped with a gas proportional detector, was used to collect the experimental diffraction patterns both for the qualitative and quantitative analysis. The incident beam pathway included a 1° divergence slit, 0.04 rad Soller slits, a 15 mm fixed mask, and a 1° anti-scatter slit. A further set of 0.04 rad Soller slits and a curved graphite monochromator were mounted in the pathway of the diffracted beam. The radiation source was a copper anode X-ray tube ( $\lambda_{\text{CuK}\alpha 1, \text{K}\alpha 2} = 1.540598, 1.544426 \text{ \AA}$ ) loaded at 40 kV and 40 mA. Nanoparticle powders were loaded in a quartz flat holder contributing zero background. XRD patterns were collected at room temperature in the 5-120 °2 $\theta$  range, with a scanning rate of 0.0025°·s<sup>-1</sup> and a step size of 0.02 °2 $\theta$  in the continuous scanning mode. The reference material used as external standard was silicon powder (Si NIST 640c), certified by National Institute of Standards and Technology (NIST) for X-ray powder diffraction.

To determine the crystallization degree, pure hematite ( $\alpha$ -Fe<sub>2</sub>O<sub>3</sub>), supplied by Metco (Metco srl, Monteveglio, Bologna, I), was used as internal standard. This phase was considered suitable as its mass absorption coefficient (MAC) (220.77 cm<sup>2</sup>/g) is comparable to that of Fe<sub>3</sub>O<sub>4</sub> (228.02 cm<sup>2</sup>/g). Mixed samples were prepared adding to Fe<sub>3</sub>O<sub>4</sub> samples about 10 wt% of  $\alpha$ -Fe<sub>2</sub>O<sub>3</sub>. The powder mixtures were homogenized by hand-grinding in an agate mortar. The phase fractions extracted by the Rietveld refinements were rescaled into absolute values on the basis of the weight of Fe<sub>3</sub>O<sub>4</sub> originally added to the mixtures and therefore internally renormalized [29]. The Rietveld refinements were obtained using the General Structure Analysis System (GSAS) software package [38] and its graphical user interface EXPGUI [39]. The starting atomic coordinates and structure factors for all phases composing the system were taken from the literature: Bosi et al. [40] for Fe<sub>3</sub>O<sub>4</sub>, Blake et al. [41] for  $\alpha$ -Fe<sub>2</sub>O<sub>3</sub>, Wyckoff [42] and NIST Certificate for silicon 640c.

Rietveld analysis was performed according to most accepted guidelines, following the four steps of analysis described in more detail by Sciancalepore et al. [32]: (i) standardization of the internal standard, (ii) determination of accurate unit cell dimensions of  $\text{Fe}_3\text{O}_4$ , (iii) structure refinement of  $\text{Fe}_3\text{O}_4$ , (iv) accurate quantitative phase analysis.

For the microstructure, the WPPM procedure, based on to the direct generation of the diffraction pattern from physical models of material structure and microstructure [33], was embodied in the general nonlinear least squares fitting software PM2K [43]. For fcc materials, such as  $\text{Fe}_3\text{O}_4$ , the generic profile (i.e., family of reflection)  $I_{\{hkl\}}$  can be represented as a Fourier integral equation (1):

$$I_{hkl}(s) = \int_{-\infty}^{\infty} C_{hkl}(L) e^{2\pi i L \cdot s} dL \quad (1)$$

where  $C_{hkl}(L)$  is the Fourier Transform (FT) related to instrument and microstructure given by (2):

$$C_{hkl}(L) = T^{IP}(L) \cdot A_{hkl}^S(L) \cdot A_{hkl}^M(L) \quad (2)$$

where  $T^{IP}(L)$  is the FT term of the instrumental profile,  $A_{hkl}^S(L)$  accounts the size effects (dimension and shape of the coherently scattering domains), and  $A_{hkl}^M(L)$  is the FT term relative to microstrain.

In particular, the instrumental function was provided by a parameterization of the profiles of a line profile standard (Si NIST 640c in the present case) described by pseudo-Voigt curves [44]; the  $A_{hkl}^S(L)$  term [34] was defined considering a lognormal distribution of spherical grains (the validity of this choice was supported by TEM); the  $A_{hkl}^M(L)$  term was evaluated by the general strain model based on a 4th order invariant form of the Miller indices [45].

### 2.3 TEM analysis

To define the morphology and the grain-size distributions, TEM (JEM 2010, Jeol, Japan) micrographs were acquired on the dried powders. In order to verify the nanoparticle elemental composition, energy dispersive X-ray spectrometry (EDS) experiments were carried out by an Oxford INCA100 microanalysis system, included in the TEM instrumental configuration. The powders were dispersed in chloroform and a drop of the obtained suspension was placed on a copper grid (200 mesh) covered with PELCO® support films of Formvar, and dried. Recorded images were analyzed using the SPIP (Scanning Probe Imaging Processor, Image Metrology A/S, Denmark) software to determine the histogram plot of the grain size distribution. A minimum of 1000 particles was measured for each powder sample to obtain a representative statistical set. The grain size was approximated by the equivalent circular diameter (or Heywood diameter, E.C.D), representing the diameter of the circle having the area equivalent to the nanoparticle area [46]. The so obtained experimental histograms was fitted by nonlinear curve-fitting tool, using OriginLab software (Microcal Software, Northhampton, USA). The grain size distribution of the MNPs was described by the log-normal distribution function, as already found for other nanostructured systems [47,48], and the histograms and the distribution curves were normalized. The log-normal function has the form expressed by the equation (3):

$$g_{LN}(D) = \frac{1}{(2\pi)^{1/2} \cdot D \sigma} e^{\left[ -\frac{1}{2} \left( \frac{\ln D - \mu}{\sigma} \right)^2 \right]} \quad (3)$$

where  $D$  is the particle diameter,  $\mu$  and  $\sigma$  are, respectively, the lognormal mean and standard deviation obtained during the fitting procedure. Using this elaboration, mean size,  $D_0$ , and standard deviation,  $SD$ , of the grain size distribution are defined respectively by equations (4a) and (4b)

$$D_0 = e^{\left(\mu + \frac{1}{2}\sigma^2\right)} \quad (4a)$$

$$SD = \left(e^{(2\mu + \sigma^2)} \cdot [e^{\sigma^2} - 1]\right)^{1/2} \quad (4b)$$

Finally, the mean volume of powder grains was calculated using the 3th moment of the distribution, according to the following relationship (5):

$$\langle V(\mu, \sigma) \rangle = \frac{\pi}{6} e^{\left(3\mu + \frac{9}{2}\sigma^2\right)} \quad (5)$$

The same expressions (4a), (4b) and (5) were used in the WPPM investigation, in order to compare the grain mean volumes, obtained by TEM image analysis, with the corresponding crystallite values, derived by WPPM.

## 2.4 Spectroscopic characterization

Sample phase composition was confirmed by Raman spectroscopy. Raman-scattering experiments were carried out using a micro-Raman system (Labram instrument Jobin Yvon-Horiba) at room temperature. The 632.81 nm line of He-Ne laser with an exposure time of 60 s was used for excitation.

In order to investigate the presence of residual organic groups on the sample surface, infrared spectroscopy (FT-IR) analyses were performed on the obtained powder. Data were recorded in the attenuated total reflectance mode with the spectrophotometer Avatar 330 (Thermo Nicolet, Germany). A minimum of 64 scans with a resolution of  $1 \text{ cm}^{-1}$  was implemented.

## 2.5 Magnetic characterization

Magnetic measurements were performed using a Lakeshore 7400 vibrating sample magnetometer (maximum field: 17 kOe) equipped with a continuous-low cryostat operating in the range 10 – 300 K. Hysteresis loops were obtained at room temperature for all samples and as functions of measurement temperature for Mag-HD\_6 sample. FC/ZFC curves were measured in all samples between 10 and 300 K under an applied field of 200 Oe at a constant  $dT/dt$  rate of about 6 K/min. All samples for magnetic measurements were prepared by compacting the as-received nanopowders in diamagnetic sample holders to avoid spurious signals related to particle displacement during a measurement.

## 3. Results and discussion

### 3.1 MNPs characterization

Independently of the precursor-to-solvent ratio, all synthesized powders appear in good agreement with the reference pattern of  $\text{Fe}_3\text{O}_4$  (ICDD file 01-075-0449). The XRD pattern of the as-obtained Mag-HD\_6 powder, chosen as a representative, is reported in Fig. 1(a). The lack of any additional reflections proves that the sample powder is a single crystalline phase, without any byproduct within the detection limit of XRD. However, the broad peaks do not allow excluding the presence of

maghemite ( $\gamma\text{-Fe}_2\text{O}_3$ ), as the two oxides have similar structure, with comparable cell parameters ( $a_{\text{maghemite}}=8.346 \text{ \AA}$  and  $a_{\text{magnetite}}=8.397 \text{ \AA}$ ) [49]. Raman spectroscopy was used to differentiate the two iron oxide phases. As shown in Fig. 2(a), the Raman spectrum of Mag-HD\_6 powder exhibits only the characteristic band of  $\text{Fe}_3\text{O}_4$  at  $670 \text{ cm}^{-1}$ , assigned to the  $A_{1g}$  transition [50], and thus allow to exclude the presence of  $\gamma\text{-Fe}_2\text{O}_3$ , independently on the precursor-to-solvent ratio used [51]. FT-IR analysis (Fig. 2(b)) showed the presence of carboxylate groups on nanoparticle surface, arising presumably from the oxidation of a hydroxyl group due to the reduction of  $\text{Fe}^{3+}$  to  $\text{Fe}^{2+}$ , and free alcoholic groups, reasonably belonging to the same coordinating molecule. In fact, the bands in  $1600\text{-}1520 \text{ cm}^{-1}$  and  $1430\text{-}1320 \text{ cm}^{-1}$  ranges can be assigned, respectively, to the asymmetrical and symmetrical vibrations of the carboxylate group [52], while the broad band at  $3300 \text{ cm}^{-1}$  is referred to the free hydroxyl group.

The structural and microstructural refinements of Mag-HD\_6 powder, provided respectively by the Rietveld-R.I.R. and WPPM methods, are presented in Fig. 1, together with the experimental diffraction pattern of the same sample. As shown by the curve fitting, the two different approaches in the XRD characterization are both effective to describe the experimental data, providing complementary information on the analyzed sample.

In the Rietveld method, to determine the content of amorphous phase, the samples were diluted with the *ad hoc* internal standard ( $\alpha\text{-Fe}_2\text{O}_3$ ). Fig. 1(b) reports the observed (cross), calculated (solid line), background (dashed line) and difference curves (dotted line) of the refined pattern, related to the last step (the final quantitative analysis) of the whole Rietveld refinement cycle for Mag-HD\_6 sample. Cubic magnetite ( $\text{Fe}^{2+}\text{Fe}_2^{3+}\text{O}_4$ ) was refined in space group  $Fd\bar{3}m$ . Although the trend is only indicative as the values are within the standard deviations, the unit cell parameter  $\bar{a}$  of the nanophasic  $\text{Fe}_3\text{O}_4$  samples decreases from  $8.387$  to  $8.381 \text{ \AA}$ , with increasing precursor-to-solvent ratio (Tab. 2). It can be speculated that the values of the calculated unit cell constant of  $\text{Fe}_3\text{O}_4$  may be related to the structural rearrangement of crystalline lattice of  $\text{Fe}_3\text{O}_4$ , as observed in other works [53] on nanophasic structures, interpreted in terms of surface relaxation [54]. The results of the QPA are reported in Tab. 2 and clearly show that the crystalline content decreases as the precursor-to-solvent is increased, ranging from  $67 \text{ wt\%}$  for Mag-HD\_1 sample to  $60 \text{ wt\%}$  for Mag-HD\_6 powder.

The XRD patterns were also modeled by WPPM (Fig. 1(c)) and the corresponding refined parameters are summarized in Tab. 2. The microstrain  $\left(\langle \varepsilon_{\{hkl\}}^2 \rangle^{\frac{1}{2}}\right)$  information, along  $[111]$  and  $[200]$  as representative crystallographic directions, is summarized by values at half-diameter distance  $L=D_0^{\text{WPPM}}/2$ , where  $D_0^{\text{WPPM}}$  is the WPPM mean diameter of the powders, obtained in different synthetic conditions. The microstrain increases, always keeping the same anisotropy (which is likely related to the intrinsic elastic anisotropy of the material), from Mag-HD\_1 to Mag-HD\_6. The microstrain behavior, which thus follows the decrease of nanoparticle size as already observed in other MNP systems [55], can reasonably be related with the non-homogeneous atomic displacement due to the grain surface relaxation. Furthermore, the anisotropy of the microstrain effect, greater along the direction  $[h00]$  compared to  $[hhh]$ , is quite usual for the elastic anisotropy of almost all similar cubic crystalline phases. In any case, the contribution of the microstrain slightly effects the peak broadening (as compared to plastically deformed systems), and can be attributed almost entirely to the nanoparticle size/surface relaxation effect.

The size distributions, extracted by WPPM, are shown in Fig. 3 (dotted line). Results show that all samples have a curve compatible with a monomodal log-normal distribution that becomes increasingly narrow and symmetrical as the precursor concentration is increased. In particular, the average size of the coherent diffraction domains decreases as the precursor concentration increases (the precursor-to-solvent ratio increases), ranging from  $11$  to  $5 \text{ nm}$  (Tab. 3).

This result is further confirmed by the nanoparticle size distribution curves, experimentally obtained by TEM dimensional

analysis (Fig. 3, solid line). Also in this elaboration, all samples present a monomodal log-normal distribution, and the dimension of the nanoparticles, as visualized by TEM images, decreases from 15 to 9 nm increasing the precursor concentration.

The crystallite dimensions, obtained by WPPM analysis, are coherent with the nanoparticle size estimated by TEM, even if grains always appear larger than the crystallites (Fig. 3(a-d) and Tab. 3). Analyzing the WPPM and TEM results, it can be put forward that grains are formed by both crystalline and amorphous phases, so that TEM mean values  $D_0^{\text{TEM}}$ , are always greater than those obtained by XRD elaboration  $D_0^{\text{WPPM}}$ , where only the crystalline fraction contributes.

In order to understand the effect of precursor-to-solvent ratio on nanoparticle crystallinity, the mean volume (as defined by eq. 5) of the grains  $\langle V \rangle_{\text{TEM}}$  and crystallites  $\langle V \rangle_{\text{WPPM}}$  are detailed in Tab. 3. The ratio between  $\langle V \rangle_{\text{TEM}}$  and  $\langle V \rangle_{\text{WPPM}}$  slightly increase as the precursor-to-solvent ratio increases: this indicates that the amorphous volume in the grains increases proportionally with the precursor-to-solvent ratio, compared to the fraction of the crystalline phase. The behavior agrees with the results obtained by the Rietveld-R.I.R. analysis, which showed that the crystallinity decreases as the precursor-to-solvent ratio increases.

According to the TEM images (Fig. 4),  $\text{Fe}_3\text{O}_4$  particles appear homogeneous and well dispersed nanometric single-crystals. Elemental composition of nano-magnetite was confirmed by EDS spectrum, in Fig. 4 (e): the detected elements, related to the nanoparticles, are just iron and oxygen, while carbon and copper peaks derive from the TEM grid. TEM micrographs, from Fig. 4(a) to (d), clearly showed that nanoparticle morphology changes and the grain size decreases as the precursor-to-solvent ratio is increased. At low precursor-to-solvent ratio nearly spherical nanocrystals are formed, with a broad range of dimensions. At higher precursor-to-solvent ratio, anisotropic crystal habits other than spherical are obtained.

This behavior was already observed for other experimental synthesis of metallic and alloy nanoparticles [56].

In our system, considering the theory of nanoparticle nucleation and growth in solution [57], at high values of precursor-to-solvent ratio, the monomer concentration in solution guarantees a high supersaturation and thus a high nucleation rate with the formation of a large number of nuclei, characterized by a smaller size. On the contrary, when the precursor-to-solvent ratio is small, the low value of the supersaturation determines a reduced nucleation rate with the formation of few nuclei with larger dimensions. Moreover, when the supersaturation level is low, the broadening of the size distribution is more marked and occurs mainly via the Ostwald ripening process.

From a synthetic point of view, this means that the nanoparticles grain and crystallite size can opportunely be tuned just by changing the precursor-to-solvent ratio without any additional organic stabilizer [58].

### 3.2 Magnetic characterization

The room-temperature magnetic hysteresis loops of all samples are reported in Fig. 5. All curves exhibit no appreciable coercive field (see inset) and can be fitted by a superposition of Langevin functions; however, low-temperature measurements (discussed below) indicate that these  $\text{Fe}_3\text{O}_4$  nanoparticles are not in the superparamagnetic phase even at room temperature, independent of the precursor concentration. The room-temperature saturation magnetization ( $M_s$ ) turns out to be a function of precursor concentration which modifies the average nanoparticle size as shown in Fig. 6 where  $M_s$  is plotted against  $1/D_0^{\text{TEM}}$ ,  $D_0^{\text{TEM}}$  being the diameter values as estimated by TEM from Tab. 3. The experimental points in the plot are remarkably aligned and are fitted by the linear law [59,60]



$$M_s(D_0^{TEM}) = M_{s-bulk} \left(1 - \frac{6t}{D_0^{TEM}}\right) \quad (6)$$

where  $M_{s-bulk}$  is the magnetization in the  $D_0^{TEM} \rightarrow \infty$  limit and  $t$  is the thickness of a “dead” magnetic layer around each magnetic nanoparticle [60]. The term “dead layer” means, in this context, a magnetically disordered, extra-hard phase whose contribution to one nanoparticle’s net magnetic moment is negligible because of spin compensation; the magnetic field needed to align the frustrated magnetic moments in the dead layer is much higher than the maximum field used in the present measurements. The magnetic disorder of the dead layer arises from competition among magnetic energies (exchange, anisotropies) affected by the symmetry breaking at the boundary of the particle [61]; as a consequence, such a layer is expected to continuously envelop a nanoparticle’s core.

Our fit gives  $M_{s-bulk} = 95 \pm 3$  emu/g, a value compatible with the room-temperature saturation magnetization of bulk  $\text{Fe}_3\text{O}_4$  ( $\cong 92$  emu/g [62]) and  $t \cong 0.6$  nm for the thickness of the disordered surface layer, in agreement with values typically found in other magnetic nanoparticle systems[59,60]. It can be concluded that the reduction of  $M_s$  with decreasing the nanoparticle size is basically determined by the surface-to-volume ratio rather than by an absolute increase in the thickness of the disordered surface layer, which is virtually unaffected by the precursor concentration used during the nanoparticle synthesis process.

The magnetic hysteresis loops of sample Mag-HD\_6 measured at different temperatures between 10 and 300 K are shown in Fig. 7 (for clarity, only the low-field region is reported in this Figure). Both the coercive field ( $H_c$ ) and the remanence-to-saturation magnetization ratio ( $M_r/M_s$ ) steadily increase with decreasing temperature and are roughly proportional to each other, as usually observed in nanogranular systems [63] (Fig. 8(a)). The saturation magnetization monotonically increases to about 69 emu/g (Fig. 8(b) with decreasing temperature; this is to be compared with the low-temperature saturation magnetization value for bulk  $\text{Fe}_3\text{O}_4$ , 98 emu/g [62]). In order to ascertain the overall magnetic behavior of this material, the reduced anhysteretic curves (basically, the average between upper and lower magnetic-loop branches normalized to saturation magnetization [64]) have been plotted in Fig. 9(a) as functions of the magnetic field-to-temperature ( $H/T$ ) ratio. In a genuine superparamagnetic (SP) material, all curves are expected to overlap [65]. Such a scaling law is never followed in the considered system, not even around room temperature. On the contrary, the so-called “interacting superparamagnet” (ISP) model, which predicts an overlap of the reduced anhysteretic magnetization ( $M/M_s$ ) curves when plotted against the magnetic field-to-saturation magnetization ( $H/M_s$ ) instead of  $H/T$  [64] is able to account for the experimental data over the whole investigated temperature range (Fig. 9(b)). This means that the individual nanoparticles in this nanopowder are substantially interacting. The ISP model depicts this magnetic interaction (believed to be mainly of dipolar origin) making use of an ad-hoc, mean-field approach [66]; the extension of the validity range of the ISP scaling law up to room temperature indicates that interparticle interaction is quite large in Mag-HD\_6, in spite of the presence of a dead layer around particles. It is expected that the same picture applies to all examined nanopowders, this view being corroborated by the field cooled and zero-field cooled (FC/ZFC) curves reported in Fig. 10(a). For clarity, the curves were normalized to the value taken at 300 K. None of the FC/ZFC curve pairs is characterized by the typical shape one expects for non-interacting magnetic nanoparticles. In particular, the FC curves of samples Mag-HD\_4 and Mag-HD\_6 are nearly flat over the entire temperature range, while the FC curves for samples Mag-HD\_1 and Mag-HD\_2 display a slight tendency to decrease with increasing temperature up to about 25 K; above, both curves increase almost linearly. On the other hand, all ZFC curves (with the exception of the one measured in Mag-HD\_6) show no maxima at intermediate temperatures and merge with the

corresponding FC curves around room temperature. Such a behavior indicates a ferromagnetic-like response of the magnetic nanoparticles, being qualitatively similar to the trends observed in highly correlated nanoparticle systems where collective effects occur [67]. As a consequence, FC/ZFC curves cannot be safely exploited to provide an independent estimate of the nanoparticle size. The only exception is provided by Mag-HD\_6 nanoparticles which are characterized by a ZFC curve showing a broad and weak maximum at  $T_M \cong 240$  K, just before merging with the corresponding FC curve. In this case, it is possible to make use of a standard analysis [68] to get a rough estimate of the size  $D$  of the individual nanoscale entities undergoing blocking when the temperature is decreased. Such a procedure exploits the temperature difference  $\Delta(T)$  between experimental FC and ZFC curves; the  $p(D)$  distribution function is given by the equation (7):

$$p(D) = \frac{\pi}{2} \frac{|K_{\text{eff}}(T)|}{25k_B} D^2 p(T_B \rightarrow D) \quad (7)$$

where  $|K_{\text{eff}}|$  is the magnitude of the overall anisotropy energy in a nanoparticle [60],[69],  $p(T_B) \cong -\frac{d\Delta(T)}{dT}\bigg|_{T=T_B}$  and the relation between  $T_B$  and  $D$  is given by  $D = \left(\frac{6}{\pi} \frac{25k_B}{|K_{\text{eff}}(T)|} T_B\right)^{\frac{1}{3}}$  [69]. The temperature dependence of the magnetic anisotropy  $K_{\text{eff}}$  theoretically obtained by Yanes et al. [70] has been used, with  $K_{\text{eff}}(T = 4 \text{ K}) \cong 2.5 \times 10^5 \text{ erg/cm}^3$  [71]. The resulting, almost Gaussian  $p(D)$  distribution is shown in Fig. 10(b) (full symbols) along with the corresponding log-normal curve obtained from TEM analysis (Fig. 3 (d) and Fig. 4 (d)). The striking difference between the two curves suggests that the individual nanoscale entities which undergo blocking are not individual nanoparticles, being instead aggregates of correlated nanoparticles extending to about 28 nm in diameter and whose mean size is  $D_{0 \text{ (FC/ZFC)}} = 13.6 \text{ nm}$ . This result is in agreement with the observation that Mag-HD\_6 nanopowder does not follow the standard SP scaling behavior, as previously discussed; the shape of FC/ZFC curves suggests a fortiori that the same conclusion can be drawn for all the other nanopowders.

The onset of a correlated, ferromagnetic-like response in samples Mag-HD\_1/2/4 is explained considering that dipolar interaction is proportional to the quantity  $\mu^2/d^3 \equiv N\mu^2$  where  $\mu$  is the mean nanoparticle magnetic moment,  $d$  the interparticle distance,  $N$  the number of nanoparticles per unit volume; such a quantity is in turn equal to  $M_s\mu$  and is therefore proportional to the product  $M_sV$ ,  $V$  being the mean nanoparticle volume. In fact, both  $V$  and  $M_s$  increase as the precursor-to-solvent ratio decreases (Tab. 3 and Fig. 6), so that the overall interaction energy is expected to steadily increase from sample Mag-HD\_6 to sample Mag-HD\_1.

These results may be compared with the recent findings by other groups who are working on similar particles prepared by different chemical techniques. Citric/ascorbic acid-coated magnetite nanoparticles characterized by slightly smaller average diameters (as determined by TEM histograms) display a broad but definite maximum with a merging of ZFC and FC curves immediately below room temperature, as in our sample Mag-HD\_6 [72]. Similarly, oleic-acid coated magnetite nanoparticles show a sharp maximum of the ZFC curve when their size is between 5 and 8 nm, and a much broader maximum when their size approaches the one of sample Mag-HD\_6 [73]. An exhaustive work on magnetic interaction effects in magnetite nanoparticle systems [74] shows how the shape of FC/ZFC curves is affected by interactions; an independent model of the role of interactions has been recently proposed [75]; the conclusions of both papers strengthen the interpretation given here. The effect of a different alkanediol solvent (1,2-octanediol) on the magnetic properties of magnetite nanoparticles has been recently examined [76]; in that case, although a core-shell structure comprised of two

crystallographically and magnetically different phases is observed within a nanoparticle, the measured magnetic properties are comparable to the ones discussed in this paper and the obtained nanoparticles are clearly demonstrated to be interacting.

#### 4. Conclusions

In this work, the formation of highly crystalline  $\text{Fe}_3\text{O}_4$  nanocrystals (ranging from 15 to 9 nm) was obtained by one-pot NHSG reaction between iron(III)-acetylacetonate, as metal precursor, and 2-ethyl-1,3-hexanediol, as reactive solvent. The XRD, TEM and spectroscopic data analysis showed that, in the studied conditions, increasing the precursor-to-solvent ratio a decrease of  $\text{Fe}_3\text{O}_4$  crystallinity, crystallite size and cell parameter range associated with an increase of microstrain were observed. The amorphous phase is presumably constituted by both amorphous oxide and organic chain present on the particle surfaces as highlighted by IR analysis.

The magnetic behavior of the nanopowders can be understood by considering that magnetic interparticle interactions (basically, of dipolar nature) induce a collective response of nanoparticles despite the presence of a thin (0.6 nm) magnetically dead layer at the surface. In sample Mag-HD\_6 the magnetic aggregates are estimated to contain less than 10 nanoparticles; in the other samples the degree of magnetic correlation of nanoparticles is larger, leading to extensive magnetic aggregates exhibiting a ferromagnetic-like response. In fact, dipolar interaction increases as the precursor-to-solvent ratio decreases, and more regular nanoparticles favor magnetic aggregations. The magnetically dead surface layer arises from competing magnetic interactions among surface magnetic moments; although structural data point to the existence of an amorphous phase in these nanoparticles, the evidence of a magnetically dead layer cannot be used to infer that such a phase appears in the form of a continuous shell.

## References

- [1] Y.-w. Jun, J.-w. Seo, J. Cheon, Nanoscaling Laws of Magnetic Nanoparticles and Their Applicabilities in Biomedical Sciences, *Accounts of Chemical Research*, 41 (2008) 179-189.
- [2] A.P. Alivisatos, Nanocrystals: Building blocks for modern materials design, *Endeavour*, 21 (1997) 56-60.
- [3] M.A. El-Sayed, Small Is Different: Shape-, Size-, and Composition-Dependent Properties of Some Colloidal Semiconductor Nanocrystals, *Accounts of Chemical Research*, 37 (2004) 326-333.
- [4] Y.-w. Jun, Y.-M. Huh, J.-s. Choi, J.-H. Lee, H.-T. Song, KimKim, S. Yoon, K.-S. Kim, J.-S. Shin, J.-S. Suh, J. Cheon, Nanoscale Size Effect of Magnetic Nanocrystals and Their Utilization for Cancer Diagnosis via Magnetic Resonance Imaging, *Journal of the American Chemical Society*, 127 (2005) 5732-5733.
- [5] K.R. Reddy, W. Park, B.C. Sin, J. Noh, Y. Lee, Synthesis of electrically conductive and superparamagnetic monodispersed iron oxide-conjugated polymer composite nanoparticles by in situ chemical oxidative polymerization, *Journal of Colloid and Interface Science*, 335 (2009) 34-39.
- [6] J.-I. Park, J. Cheon, Synthesis of "Solid Solution" and "Core-Shell" Type Cobalt-Platinum Magnetic Nanoparticles via Transmetalation Reactions, *Journal of the American Chemical Society*, 123 (2001) 5743-5746.
- [7] J.-I. Park, M.G. Kim, Y.-w. Jun, J.S. Lee, W.-r. Lee, J. Cheon, Characterization of Superparamagnetic "Core-Shell" Nanoparticles and Monitoring Their Anisotropic Phase Transition to Ferromagnetic "Solid Solution" Nanoalloys, *Journal of the American Chemical Society*, 126 (2004) 9072-9078.
- [8] S. Sun, C.B. Murray, D. Weller, L. Folks, A. Moser, Monodisperse FePt Nanoparticles and Ferromagnetic FePt Nanocrystal Superlattices, *Science*, 287 (2000) 1989-1992.
- [9] K.R. Reddy, K.-P. Lee, A.I. Gopalan, Novel electrically conductive and ferromagnetic composites of poly(aniline-co-aminonaphthalenesulfonic acid) with iron oxide nanoparticles: Synthesis and characterization, *Journal of Applied Polymer Science*, 106 (2007) 1181-1191.
- [10] G. Barrera, C. Sciancalepore, M. Messori, P. Allia, P. Tiberto, F. Bondioli, Magnetite-epoxy nanocomposites obtained by the reactive suspension method: Microstructural, thermo-mechanical and magnetic properties, *European Polymer Journal*, 94 (2017) 354-365.
- [11] K.R. Reddy, K.-P. Lee, J.Y. Kim, Y. Lee, Self-Assembly and Graft Polymerization Route to Monodispersed Fe<sub>3</sub>O<sub>4</sub>@SiO<sub>2</sub>-Polyaniline Core-Shell Composite Nanoparticles: Physical Properties, *Journal of Nanoscience and Nanotechnology*, 8 (2008) 5632-5639.
- [12] A. Akbarzadeh, M. Samiei, S. Davaran, Magnetic nanoparticles: preparation, physical properties, and applications in biomedicine, *Nanoscale Research Letters*, 7 (2012) 144-144.
- [13] G.E. Fryxell, G. Cao, *Environmental Applications of Nanomaterials: Synthesis, Sorbents and Sensors*, 2012.
- [14] T. Hyeon, Chemical synthesis of magnetic nanoparticles, *Chemical Communications*, (2003) 927-934.
- [15] P. Posocco, Y.M. Hassan, I. Barandiaran, G. Kortaberria, S. Priol, M. Fermeiglia, Combined Mesoscale/Experimental Study of Selective Placement of Magnetic Nanoparticles in Diblock Copolymer Films via Solvent Vapor Annealing, *The Journal of Physical Chemistry C*, 120 (2016) 7403-7411.
- [16] A.H. Latham, M.E. Williams, Controlling Transport and Chemical Functionality of Magnetic Nanoparticles, *Accounts of Chemical Research*, 41 (2008) 411-420.
- [17] A.-H. Lu, E.L. Salabas, F. Schüth, *Magnetic Nanoparticles: Synthesis, Protection, Functionalization, and Application*, *Angewandte Chemie International Edition*, 46 (2007) 1222-1244.
- [18] S. Laurent, D. Forge, M. Port, A. Roch, C. Robic, L. Vander Elst, R.N. Muller, Magnetic Iron Oxide Nanoparticles: Synthesis, Stabilization, Vectorization, Physicochemical Characterizations, and Biological Applications, *Chemical Reviews*, 108 (2008) 2064-2110.

- [19] M. Niederberger, Nonaqueous Sol–Gel Routes to Metal Oxide Nanoparticles, *Accounts of Chemical Research*, 40 (2007) 793-800.
- [20] M. Niederberger, G. Garnweitner, J. Buha, J. Polleux, J. Ba, N. Pinna, Nonaqueous synthesis of metal oxide nanoparticles: Review and indium oxide as case study for the dependence of particle morphology on precursors and solvents, *Journal of Sol-Gel Science and Technology*, 40 (2006) 259-266.
- [21] C. Sciancalepore, R. Rosa, G. Barrera, P. Tiberto, P. Allia, F. Bondioli, Microwave-assisted nonaqueous sol–gel synthesis of highly crystalline magnetite nanocrystals, *Materials Chemistry and Physics*, 148 (2014) 117-124.
- [22] N. Pinna, G. Neri, M. Antonietti, M. Niederberger, Nonaqueous Synthesis of Nanocrystalline Semiconducting Metal Oxides for Gas Sensing, *Angewandte Chemie International Edition*, 43 (2004) 4345-4349.
- [23] M. Niederberger, N. Pinna, J. Polleux, M. Antonietti, A General Soft-Chemistry Route to Perovskites and Related Materials: Synthesis of BaTiO<sub>3</sub>, BaZrO<sub>3</sub>, and LiNbO<sub>3</sub> Nanoparticles, *Angewandte Chemie International Edition*, 43 (2004) 2270-2273.
- [24] N. Pinna, M. Karmaoui, M.-G. Willinger, The “benzyl alcohol route”: An elegant approach towards doped and multimetal oxide nanocrystals, *Journal of Sol-Gel Science and Technology*, 57 (2010) 323-329.
- [25] C. Sciancalepore, F. Bondioli, M. Messori, Non-hydrolytic sol–gel synthesis and reactive suspension method: an innovative approach to obtain magnetite–epoxy nanocomposite materials, *Journal of Sol-Gel Science and Technology*, (2016) 1-15.
- [26] S.P. Gubin, *Magnetic Nanoparticles*, Wiley, 2009.
- [27] P. Panissod, M. Drillon, Magnetic Ordering due to Dipolar Interaction in Low Dimensional Materials, *Magnetism: Molecules to Materials*, Wiley-VCH Verlag GmbH & Co. KGaA, 2003, pp. 233-270.
- [28] M. Bellotto, C. Cristiani, Quantitative X-Ray Diffraction Rietveld Analysis of Low Temperature Coal Ashes, *Materials Science Forum*, 79-82 (1991) 6.
- [29] A. Gualtieri, Accuracy of XRPD QPA using the combined Rietveld-RIR method, *Journal of Applied Crystallography*, 33 (2000) 267-278.
- [30] A. Gualtieri, G. Artioli, Quantitative determination of chrysotile asbestos in bulk materials by combined Rietveld and RIR methods, *Powder Diffraction*, 10 (1995) 269-277.
- [31] D.M. Tobaldi, R.C. Pullar, A.F. Gualtieri, M.P. Seabra, J.A. Labrincha, Phase composition, crystal structure and microstructure of silver and tungsten doped TiO<sub>2</sub> nanopowders with tuneable photochromic behaviour, *Acta Materialia*, 61 (2013) 5571-5585.
- [32] C. Sciancalepore, F. Bondioli, T. Manfredini, A. Gualtieri, Quantitative phase analysis and microstructure characterization of magnetite nanocrystals obtained by microwave assisted non-hydrolytic sol–gel synthesis, *Materials Characterization*, 100 (2015) 88-97.
- [33] P. Scardi, M. Leoni, Whole powder pattern modelling, *Acta Crystallographica Section A*, 58 (2002) 190-200.
- [34] P. Scardi, M. Leoni, Diffraction line profiles from polydisperse crystalline systems, *Acta Crystallographica Section A*, 57 (2001) 604-613.
- [35] M. Sangermano, P. Allia, P. Tiberto, G. Barrera, F. Bondioli, N. Florini, M. Messori, Photo-Cured Epoxy Networks Functionalized With Fe<sub>3</sub>O<sub>4</sub> Generated by Non-hydrolytic Sol–Gel Process, *Macromolecular Chemistry and Physics*, 214 (2013) 508-516.
- [36] N. Pinna, S. Grancharov, P. Beato, P. Bonville, M. Antonietti, M. Niederberger, Magnetite Nanocrystals: Nonaqueous Synthesis, Characterization, and Solubility, *Chemistry of Materials*, 17 (2005) 3044-3049.
- [37] M. Niederberger, N. Pinna, *Metal Oxide Nanoparticles in Organic Solvents: Synthesis, Formation, Assembly and Application*, Springer London, 2009.
- [38] A.C. Larson, R.B. Von Dreele, General Structure Analysis System (GSAS), Los Alamos National Laboratory, Report LAUR 86-748 (2004).
- [39] B. Toby, EXPGUI, a graphical user interface for GSAS, *Journal of Applied Crystallography*, 34 (2001) 210-213.
- [40] F. Bosi, U. Hålenius, H. Skogby, Crystal chemistry of the magnetite-ulvöspinel series, *American Mineralogist*, 94 (2009) 181-189.
- [41] R.L. Blake, R.E. Hessevick, T. Zoltai, L.W. Finger, Refinement of the hematite structure, *American mineralogist*, 51 (1966) 7.
- [42] R.W.G. Wyckoff, *Crystal Structures*, Wiley, 1963.
- [43] M. Leoni, T. Confente, P. Scardi, PM2K: a flexible program implementing Whole Powder Pattern Modelling, *Zeitschrift für Kristallographie Supplements*, 06 (2006) 5.
- [44] P. Scardi, M. Leoni, Fourier modelling of the anisotropic line broadening of X-ray diffraction profiles due to line and plane lattice defects, *Journal of Applied Crystallography*, 32 (1999) 671-682.
- [45] A. Leonardi, P. Scardi, Dislocation Effects on the Diffraction Line Profiles from Nanocrystalline Domains, *Metallurgical*

and Materials Transactions A, (2015) 1-11.

- [46] R. Xu, O.A. Di Guida, Comparison of sizing small particles using different technologies, *Powder Technology*, 132 (2003) 145-153.
- [47] V. Haas, R. Birringer, The morphology and size of nanostructured Cu, Pd and W generated by sputtering, *Nanostructured Materials*, 1 (1992) 491-504.
- [48] C.G. Granqvist, R.A. Buhrman, Ultrafine metal particles, *Journal of Applied Physics*, 47 (1976) 2200-2219.
- [49] A.M. Jubb, H.C. Allen, Vibrational Spectroscopic Characterization of Hematite, Maghemite, and Magnetite Thin Films Produced by Vapor Deposition, *ACS Applied Materials & Interfaces*, 2 (2010) 2804-2812.
- [50] T.J. Daou, G. Pourroy, S. Bégin-Colin, J.M. Grenèche, C. Ulhaq-Bouillet, P. Legaré, P. Bernhardt, C. Leuvrey, G. Rogez, Hydrothermal Synthesis of Monodisperse Magnetite Nanoparticles, *Chemistry of Materials*, 18 (2006) 4399-4404.
- [51] R. Frison, G. Cernuto, A. Cervellino, O. Zaharko, G.M. Colonna, A. Guagliardi, N. Masciocchi, Magnetite–Maghemite Nanoparticles in the 5–15 nm Range: Correlating the Core–Shell Composition and the Surface Structure to the Magnetic Properties. A Total Scattering Study, *Chemistry of Materials*, 25 (2013) 4820-4827.
- [52] Y. Lu, J.D. Miller, Carboxyl Stretching Vibrations of Spontaneously Adsorbed and LB-Transferred Calcium Carboxylates as Determined by FTIR Internal Reflection Spectroscopy, *Journal of Colloid and Interface Science*, 256 (2002) 41-52.
- [53] C.-C. Huang, C.-Y. Tsai, H.-S. Sheu, K.-Y. Chuang, C.-H. Su, U.S. Jeng, F.-Y. Cheng, C.-H. Su, H.-Y. Lei, C.-S. Yeh, Enhancing Transversal Relaxation for Magnetite Nanoparticles in MR Imaging Using Gd<sup>3+</sup>-Chelated Mesoporous Silica Shells, *ACS Nano*, 5 (2011) 3905-3916.
- [54] P.M. Diehm, P. Ágoston, K. Albe, Size-Dependent Lattice Expansion in Nanoparticles: Reality or Anomaly?, *ChemPhysChem*, 13 (2012) 2443-2454.
- [55] D. Fiorani, *Surface Effects in Magnetic Nanoparticles*, Springer US, 2006.
- [56] J. Turkevich, Colloidal gold. Part I, *Gold Bulletin*, 18 (1985) 86-91.
- [57] Y. Yin, A.P. Alivisatos, Colloidal nanocrystal synthesis and the organic-inorganic interface, *Nature*, 437 (2005) 664-670.
- [58] I. Bilecka, I. Djerdj, M. Niederberger, One-minute synthesis of crystalline binary and ternary metal oxide nanoparticles, *Chemical Communications*, (2008) 886-888.
- [59] C. Daniela, C. Gabriel, J.O.C. Charles, Magnetic properties of variable-sized Fe<sub>3</sub>O<sub>4</sub> nanoparticles synthesized from non-aqueous homogeneous solutions of polyols, *Journal of Physics D: Applied Physics*, 40 (2007) 5801.
- [60] J.P. Chen, C.M. Sorensen, K.J. Klabunde, G.C. Hadjipanayis, E. Devlin, A. Kostikas, Size-dependent magnetic properties of MnFe<sub>2</sub>O<sub>4</sub> fine particles synthesized by coprecipitation, *Physical Review B*, 54 (1996) 9288-9296.
- [61] Y.A. Koksharov, *Magnetism of Nanoparticles: Effects of Size, Shape, and Interactions*, *Magnetic Nanoparticles*, Wiley-VCH Verlag GmbH & Co. KGaA, 2009, pp. 197-254.
- [62] B.D. Cullity, C.D. Graham, *Introduction to Magnetic Materials*, Wiley, 2011.
- [63] P. Allia, M. Coisson, P. Tiberto, F. Vinai, M. Knobel, Magnetic hysteresis in granular CuCo alloys, *Journal of Applied Physics*, 85 (1999) 4343-4345.
- [64] P. Allia, M. Coisson, P. Tiberto, F. Vinai, M. Knobel, M.A. Novak, W.C. Nunes, Granular Cu-Co alloys as interacting superparamagnets, *Physical Review B*, 64 (2001) 144420.
- [65] J.M.D. Coey, D. Khalafalla, Superparamagnetic γ-Fe<sub>2</sub>O<sub>3</sub>, *physica status solidi (a)*, 11 (1972) 229-241.
- [66] P. Allia, Fe-oxide Nanoparticles: a natural playground for testing the ISP model, *Journal of Physics: Conference Series*, 521 (2014) 012008.
- [67] F. Jiménez-Villacorta, C. Prieto, Magnetic properties and interaction mechanisms of iron-based core–shell structures prepared by sputtering at low substrate temperatures, *Journal of Physics: Condensed Matter*, 20 (2008) 085216.
- [68] H. Mamiya, M. Ohnuma, I. Nakatani, T. Furubayashim, Extraction of blocking temperature distribution from zero-field-cooled and field-cooled magnetization curves, *IEEE Transactions on Magnetics*, 41 (2005) 3394-3396.
- [69] M. Knobel, W.C. Nunes, L.M. Socolovsky, E. De Biasi, J.M. Vargas, J.C. Denardin, Superparamagnetism and Other Magnetic Features in Granular Materials: A Review on Ideal and Real Systems, *Journal of Nanoscience and Nanotechnology*, 8 (2008) 2836-2857.
- [70] R. Yanes, O. Chubykalo-Fesenko, R.F.L. Evans, R.W. Chantrell, Temperature dependence of the effective anisotropies in magnetic nanoparticles with Néel surface anisotropy, *Journal of Physics D: Applied Physics*, 43 (2010) 474009.
- [71] K. Abe, Y. Miyamoto, S. Chikazumi, Magnetocrystalline Anisotropy of Low Temperature Phase of Magnetite, *Journal of the Physical Society of Japan*, 41 (1976) 1894-1902.
- [72] N. Saxena, M. Singh, Efficient synthesis of superparamagnetic magnetite nanoparticles under air for biomedical applications, *Journal of Magnetism and Magnetic Materials*, 429 (2017) 166–176.
- [73] K. Chesnel, M. Trevino, Y. Cai, J. M. Hancock, S. J. Smith and R. G. Harrison, Particle size effects on the magnetic behaviour of 5 to 11 nm Fe<sub>3</sub>O<sub>4</sub> nanoparticles coated with oleic acid, *Journal of Physics: Conference Series* 521 (2014) 012004.

- [74] O. Moscoso-Londoño, P. Tancredi, D. Muraca, P. Mendoza Zélis, D. Coral, M.B. Fernández van Raap, U. Wolff, V. Neu, C. Damm, C.L.P. de Oliveira, K.R. Pirota, M. Knobel, L.M. Socolovsky, Different approaches to analyze the dipolar interaction effects on diluted and concentrated granular superparamagnetic systems, *Journal of Magnetism and Magnetic Materials* 428 (2017) 105–118.
- [75] D.A. Balaev, S.V. Semenov, A.A. Dubrovskiy, S.S. Yakushkin, V.L. Kirillov, O.N. Martyanov, Superparamagnetic blocking of an ensemble of magnetite nanoparticles upon interparticle interactions, *Journal of Magnetism and Magnetic Materials* 440 (2017) 199–202.
- [76] F.B. Effenberger, A.W. Carbonari, L.M. Rossi, The influence of 1,2-alkanediols on the crystallinity of magnetite nanoparticles, *Journal of Magnetism and Magnetic Materials* 417 (2016) 49–55.

**Table 1** Code and composition of the NHSG reaction batches for the magnetic nanoparticle synthesis

Sample Name	Fe(AcAc) <sub>3</sub> (g)	HD (g)	Ratio Fe(AcAc) <sub>3</sub> /HD (mol/mol)
Mag-HD_1	1	9,3	0,04
Mag-HD_2	1	4,6	0,09
Mag-HD_4	1	2,3	0,18
Mag-HD_6	1	1,5	0,27

**Table 2** The results of Rietveld refinements and the fitting parameters of the log-normal distribution functions, as obtained by WPPM analysis ( $\mu$  and  $\sigma$  are respectively the lognormal mean and standard deviation, while  $\langle \varepsilon_{\{hkl\}}^2 \rangle^{\frac{1}{2}}$  is the microstrain along the specified crystallographic direction).

Sample name	RIETVELD		WPPM			
	Crystalline Content [%]	Unit Cell Parameter [Å]	$\mu$	$\sigma$	$\langle \varepsilon_{\{111\}}^2 \rangle^{\frac{1}{2}}$	$\langle \varepsilon_{\{200\}}^2 \rangle^{\frac{1}{2}}$
Mag-HD_1	67.2(9)	8.388(2)	2.38	0.38	0.0007	0.0013
Mag-HD_2	65.0(9)	8.384(2)	2.00	0.43	0.0020	0.0024
Mag-HD_4	62.5(9)	8.385(2)	1.73	0.46	0.0024	0.0029
Mag-HD_6	60.4(8)	8.382(2)	1.60	0.46	0.0029	0.0035

**Table 3** Mean size,  $D_0$ , standard deviation, SD, and mean volume of the grain  $\langle V \rangle$ , as obtained by WPPM and TEM analysis, and ratio between TEM and WPPM mean volumes.

Sample name	WPPM			TEM			Ratio
	$D_0^{\text{WPPM}}$ [nm]	$SD^{\text{WPPM}}$ [nm]	$\langle V \rangle^{\text{WPPM}}$ [nm <sup>3</sup> ]	$D_0^{\text{TEM}}$ [nm]	$SD^{\text{TEM}}$ [nm]	$\langle V \rangle^{\text{TEM}}$ [nm <sup>3</sup> ]	
Mag-HD_1	11.65	4.65	827	14.93	4.21	1743	2.1
Mag-HD_2	8.07	3.62	275	12.07	2.96	920	3.3
Mag-HD_4	6.28	3.06	130	10.13	2.31	545	4.2
Mag-HD_6	5.52	2.68	74	9.08	1.96	331	4.5



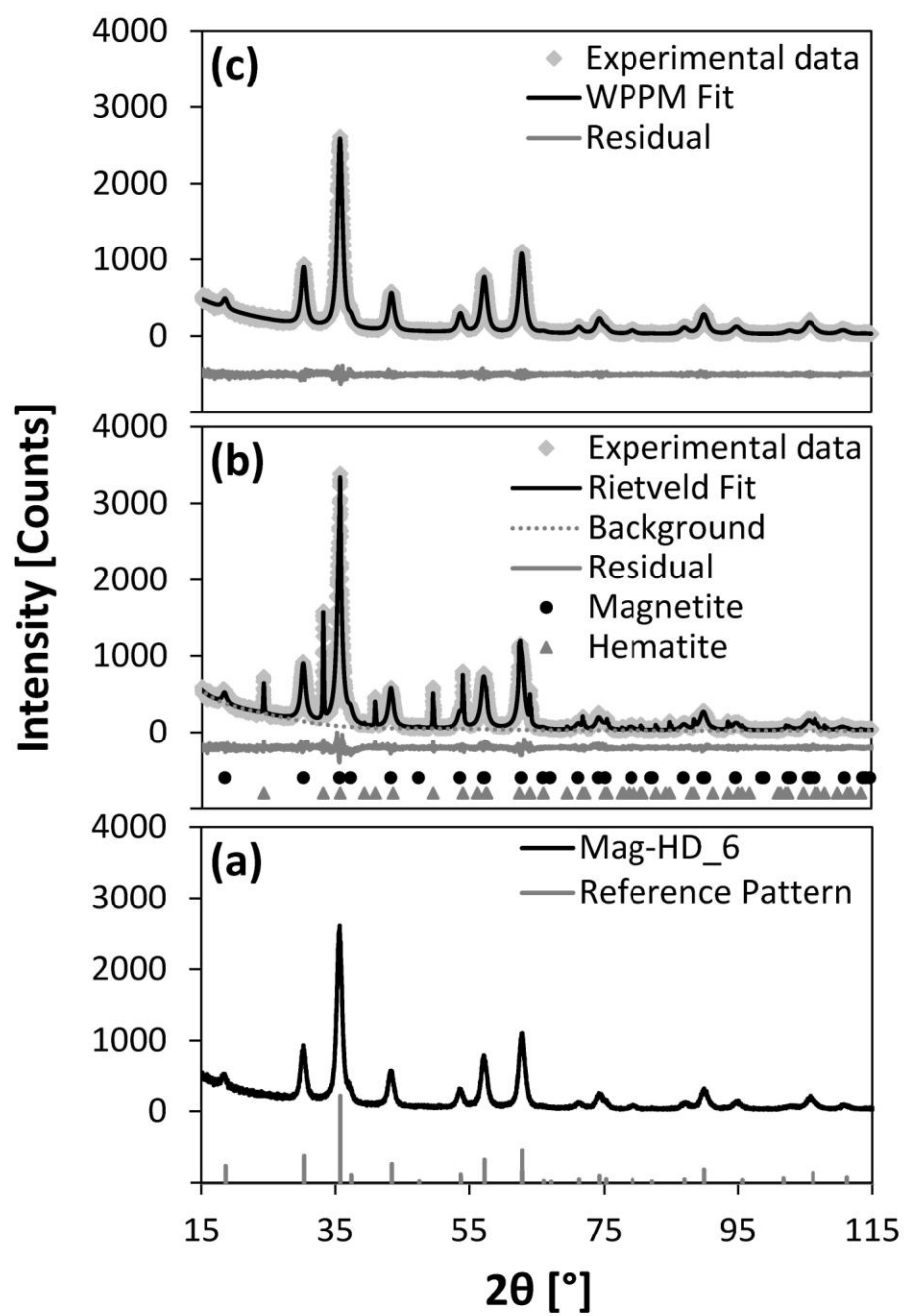


**Figure 1** XRD patterns of nanoparticle powder (a), Rietveld-RIR refinement (b) and WPPM fitting (c) for Mag-HD\_6 sample, as representative sample (Magnetite reference pattern is the JCPDS file # 01-075-0449).

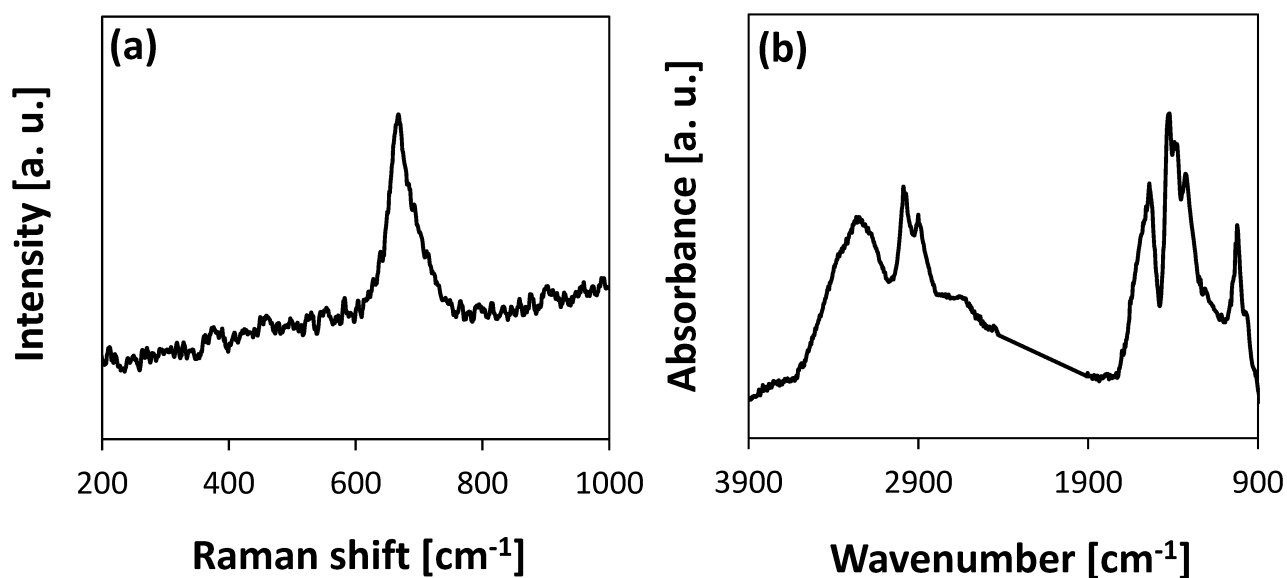


**Figure 2** Raman (a) and FT-IR (b) spectra of Mag-HD\_6 powder, as representative sample.

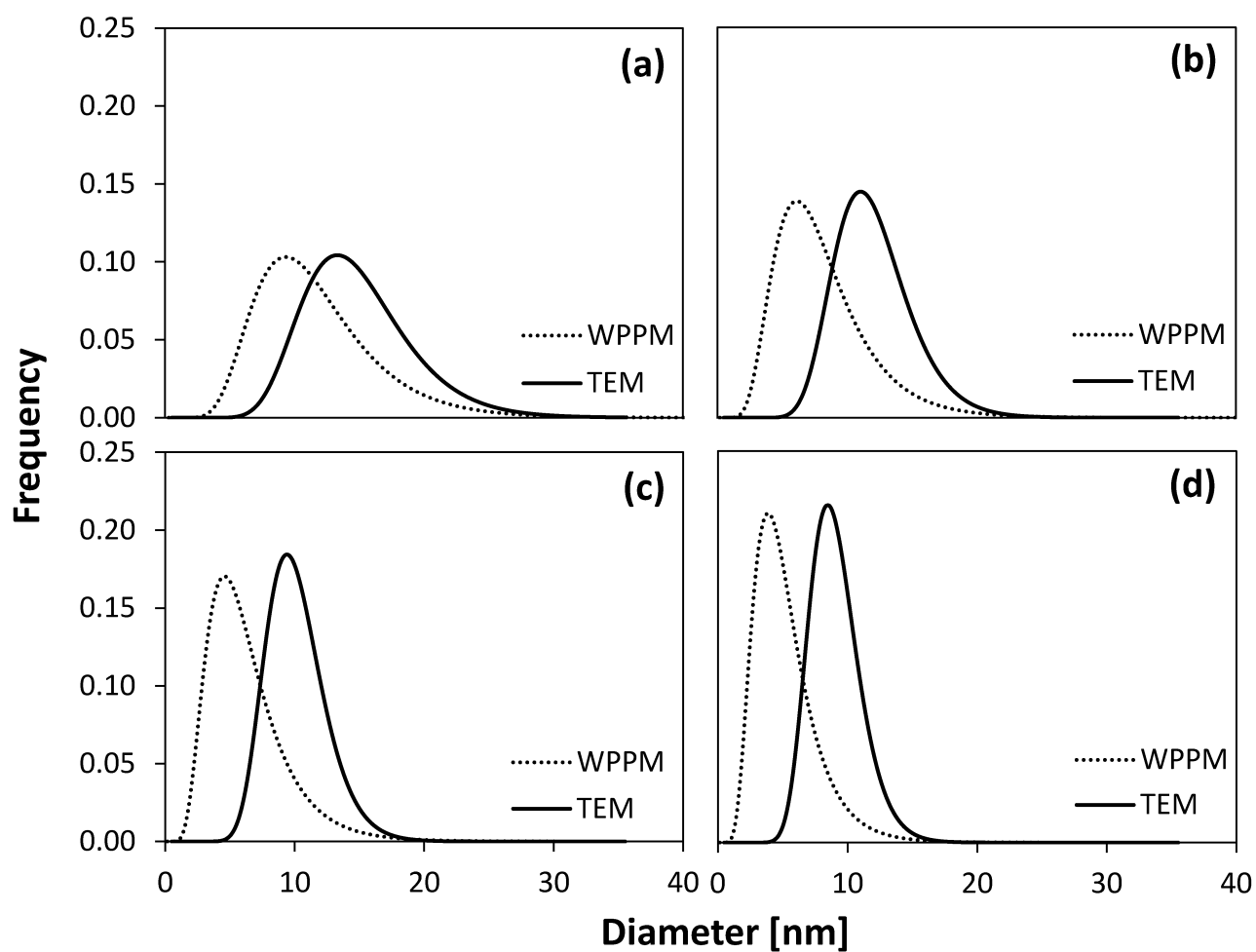


**Figure 3** Crystallite and grain size distributions, obtained respectively with WPPM and TEM method for the four powder samples: (a) Mag-HD\_1, (b) Mag-HD\_2, (c) Mag-HD\_4 and (d) Mag-HD\_6.

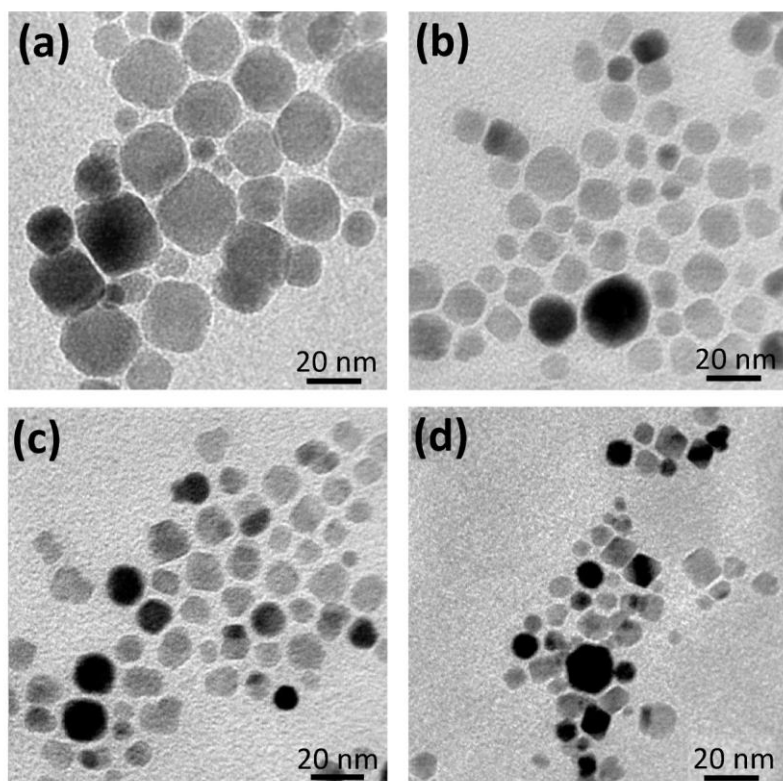


**Figure 4** TEM images of  $\text{Fe}_3\text{O}_4$  nanoparticles, obtained with HD at different precursor-to-solvent ratio: respectively Mag-HD\_1 (a), Mag-HD\_2 (b), Mag-HD\_4 (c) and Mag-HD\_6 (d).

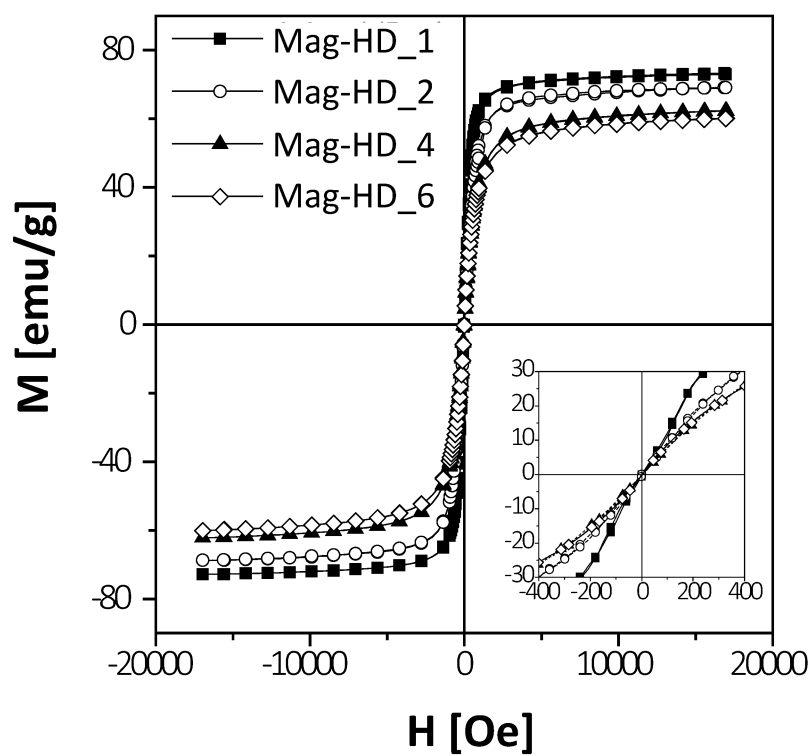


**Figure 5** Room-temperature hysteresis loops of  $\text{Fe}_3\text{O}_4$  nanoparticles prepared at different precursor concentrations.

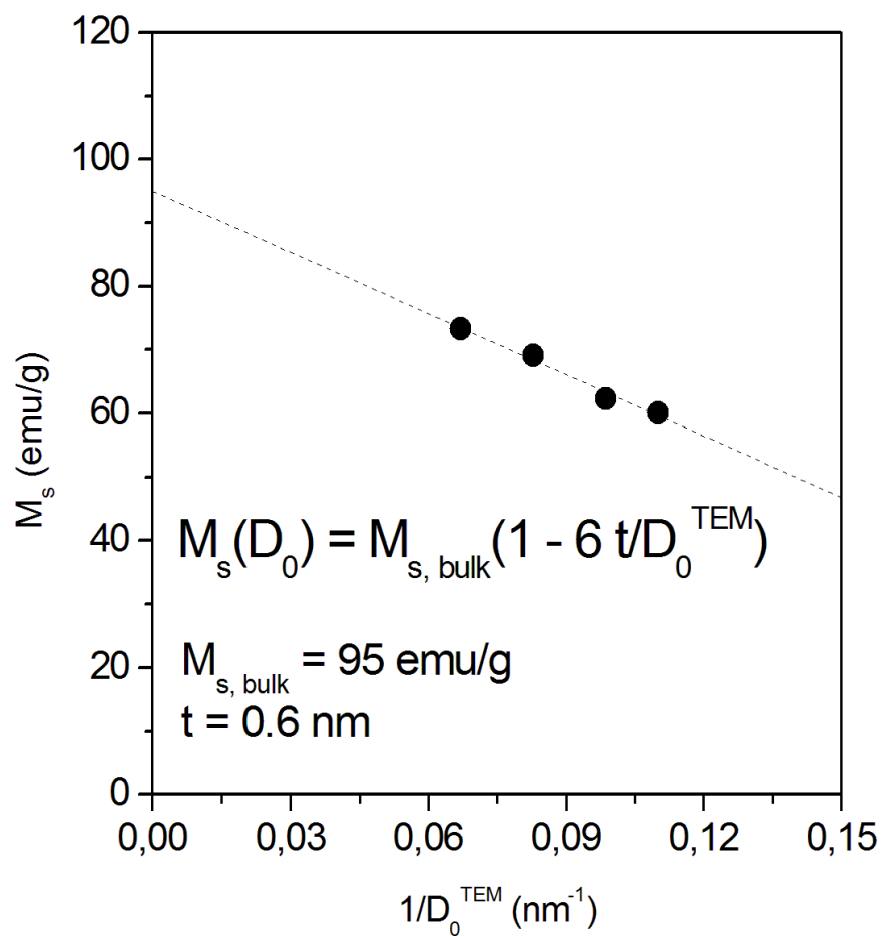


**Figure 6** Room-temperature saturation magnetization of  $\text{Fe}_3\text{O}_4$  nanoparticles as a function of the reciprocal of the mean nanoparticle size  $D_0$  as estimated by TEM measurements. The parameter  $t$  is the thickness of the disordered surface layer.

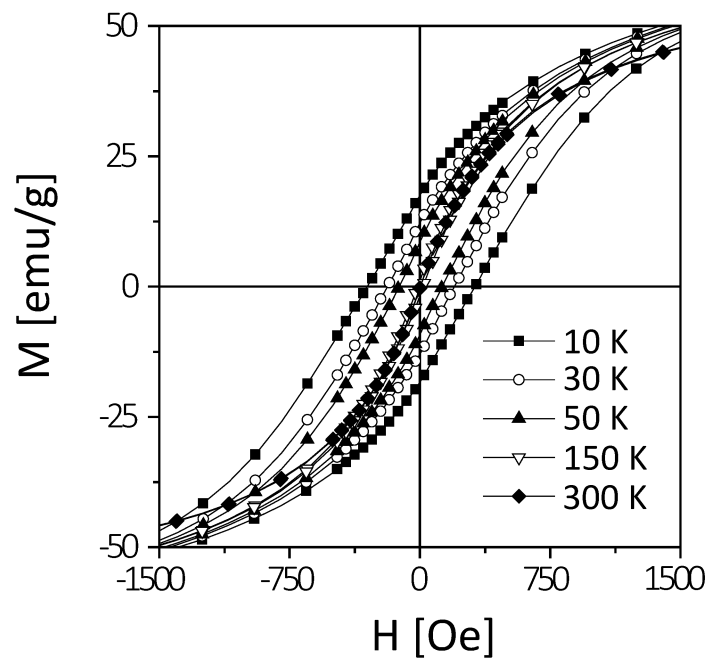


**Figure 7** Isothermal hysteresis loops at selected temperatures between 10 K and 300 K in Mag-HD\_6. The low-field region is shown.

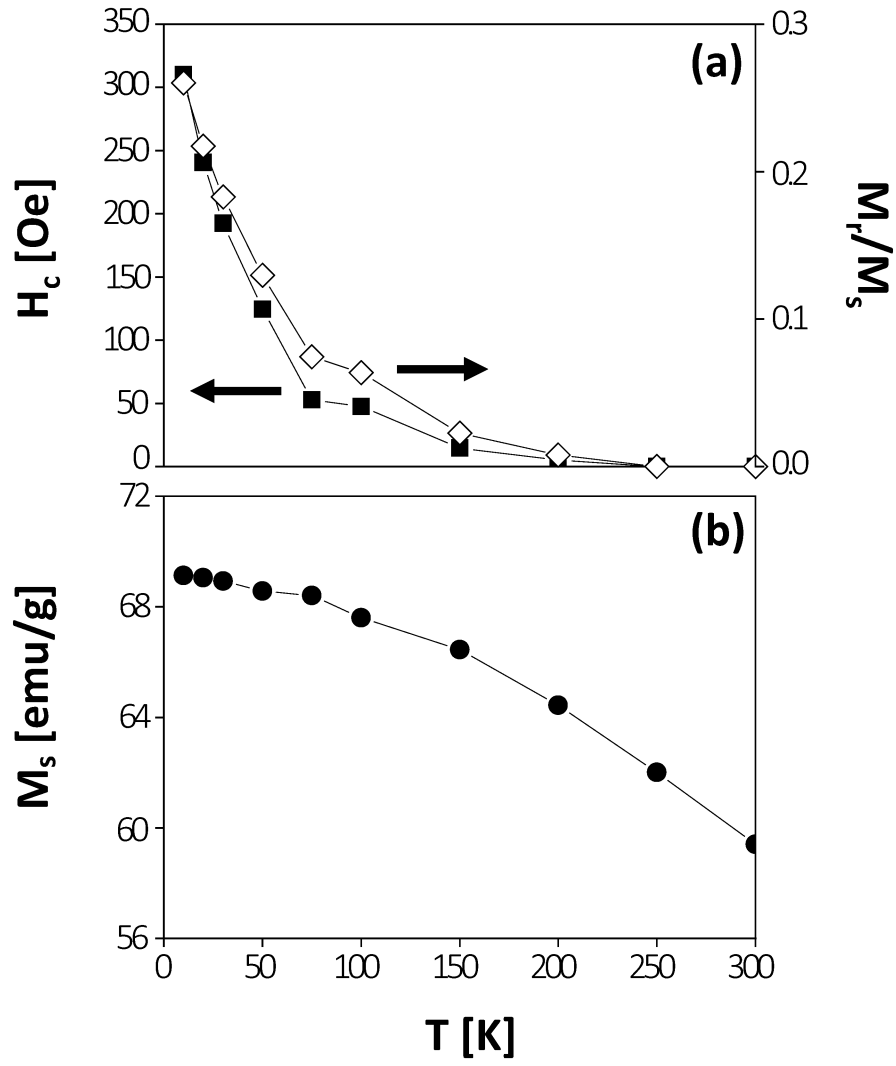


**Figure 8** Temperature behavior of the hysteresis parameters (coercive field  $H_c$  and of the remanence-to saturation ratio  $M_r/M_s$ ) in Mag-HD\_6 (a); Temperature behavior of the saturation magnetization in Mag-HD\_6 (b).

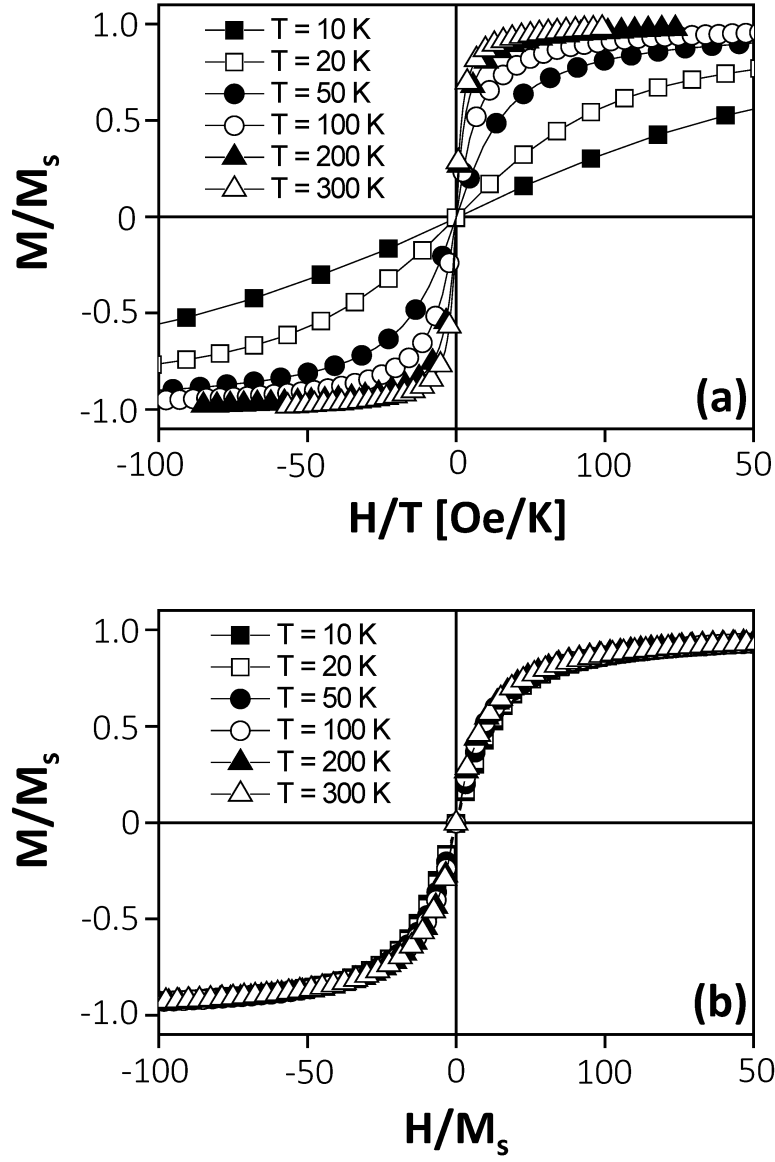


**Figure 9** Reduced anhyseretic magnetization  $M/M_s$  plotted as a function of  $H/T$  (SP scaling, (a)) and of  $H/M_s$  (ISP scaling, (b)) in Mag-HD\_6.

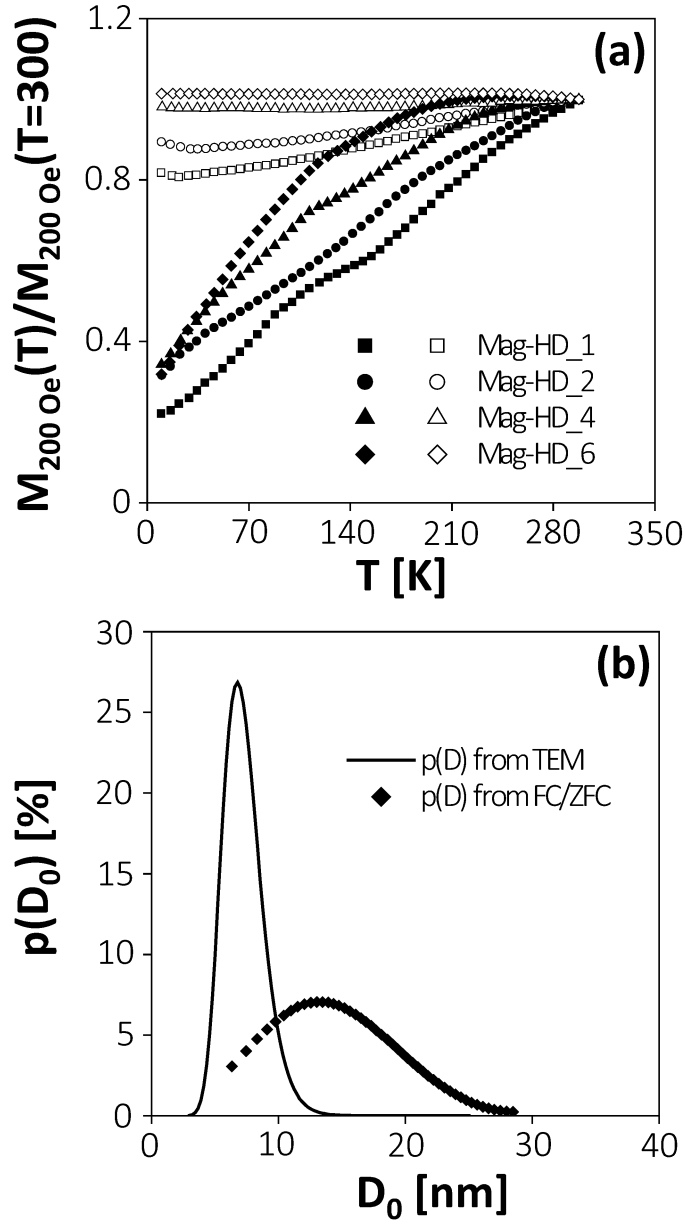


**Figure 10** FC/ZFC curves (open/full symbols, respectively ) of  $\text{Fe}_3\text{O}_4$  nanoparticles prepared at different precursor concentrations under a field of 200 Oe (a); Comparison between  $p(D)$  curve obtained by TEM measurements (line) and by FC/ZFC curve analysis (symbols) in Mag-HD\_6 (b).



